



HAL
open science

Ultrasound Computed Tomography

Philippe Lasaygues, Luis Espinosa, Simon Bernard, Philippe Petit, Régine
Guillermin

► **To cite this version:**

Philippe Lasaygues, Luis Espinosa, Simon Bernard, Philippe Petit, Régine Guillermin. Ultrasound Computed Tomography. Bone Quantitative Ultrasound, 1364, Springer International Publishing, pp.227-250, 2022, Advances in Experimental Medicine and Biology, 10.1007/978-3-030-91979-5_11 . hal-04456241

HAL Id: hal-04456241

<https://hal.science/hal-04456241v1>

Submitted on 30 Dec 2024

HAL is a multi-disciplinary open access archive for the deposit and dissemination of scientific research documents, whether they are published or not. The documents may come from teaching and research institutions in France or abroad, or from public or private research centers.

L'archive ouverte pluridisciplinaire **HAL**, est destinée au dépôt et à la diffusion de documents scientifiques de niveau recherche, publiés ou non, émanant des établissements d'enseignement et de recherche français ou étrangers, des laboratoires publics ou privés.

Chapter 11

Ultrasound Computed Tomography

Philippe Lasaygues¹, Luis Espinosa^{1,2}, Simon Bernard^{1,3}, Philippe Petit⁴, Régine Guillermin¹

¹Aix Marseille Univ., CNRS, Centrale Marseille, LMA, Marseille, France

²Univ. Toulouse 3 - Paul Sabatier, Institut Clément Ader, Tarbes, France

³University of Le Havre, CNRS, LOMC, Le Havre, France

⁴Dept. of Pediatric and Prenatal Radiology, Timone's Children-Hospital, Marseille, France

lasaygues@lma.cnrs-mrs.fr

Abstract This chapter presents theoretical, numerical, and experimental frameworks for the use of Ultrasound Computed Tomography (USCT) for cortical bone tissue imaging. Most of the research conducted on this topic concerns adult bone, although some work presented in this chapter is specific to the study of child bone. USCT is recognized as a powerful method for soft tissue imaging. In bone imaging, the difficulties arise from the very high impedance contrast between tissues which alters the propagation of the ultrasonic waves and limits the linear inversion algorithms used. Solutions consist in optimally assessing non-linear effects in an iterative approach aiming at local linearization. When the problem can be reduced to the study of a fluid-like cavity buried in an elastic cylinder surrounded by water, the signal processing and/or compound algorithms can be added as an extension to the linear algorithms. The main limitation of these methods is the heavy experimental costs involved. We have then suggested the introduction of purely numerical non-linear full-waveform inversion algorithms. The performances and the limitations of these linear and non-linear methods applied to cortical bone tissue imaging problems are overviewed and discussed.

Keywords Ultrasound computed tomography, Adapted inversion scheme, Full waveform inversion, Cortical bone shell

11.1. Introduction

B-mode pulse-echo ultrasound is a useful adult examination modality in all medical fields, with an exception of bone tissue imaging for which X-ray and magnetic resonance imaging (MRI) are preferred. For the diagnosis of diseases in children including bone pathologies, B-mode ultrasound is the privileged modality. X-ray modalities must be limited in children because of potential radiation hazards, and MRI examinations, which require sedation or anesthesia in the case of the youngest children, provide only poor cortical bone information. But pediatric ultrasound bone imaging is associated with clinical limitations. For example, current medical practice does not allow imaging under the cortical area (sub-periosteal imaging) and no information is available on the bone cortical thickness or the marrow (**Fig.11.1**).

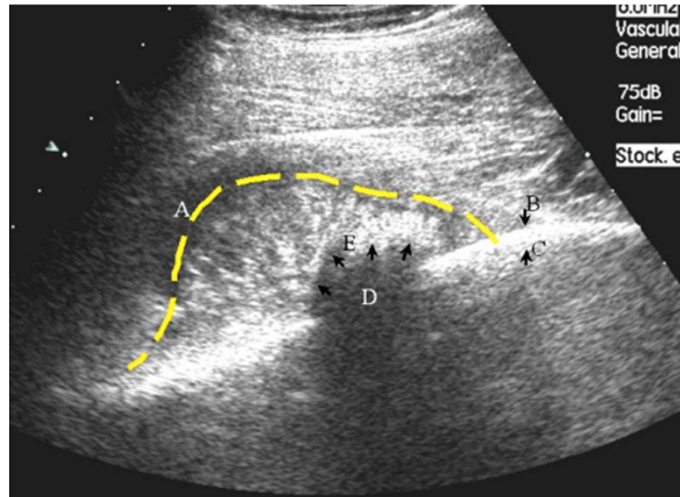


Fig.11.1 B-mode pulse-echo ultrasound image of an osteosarcoma with a periosteal reaction (sunburst appearance), [**A** Demarcation of the bone tumoral extension in the soft tissues, **B-C** Limit of the cortical area with a strong echogenicity of the interface between the periosteum and the cortical bone, **D-E** Cortical break due to the tumoral process without indications on the underlying bone structure, and the subcortical bone marrow] (courtesy of AP-HM, Marseille, France)

Recent progress in B-mode (pulse-echo) bone imaging has shown promise. By adapting the wave propagation physics to a ray-tracing model, Renaud *et al.* (Renaud *et al.* 2018) were able to estimate cortical thickness, the ultrasonic wave velocities and the anisotropy of the cortical area of a tibia and a radius, taking into account the structural heterogeneous layers of these media. The

recent advancements in the field of pulse-echo ultrasound imaging of cortical bone are covered in detail in chapter 10 of this book.

Ultrasound Computed Tomography (USCT) appears as a possible alternative to the limits of clinical B-mode ultrasound, making it possible to take into account some of the physical phenomena involved in the ultrasonic wave propagation between the probe and the inspected zone, and/or to circumvent the effects of these physical phenomena through appropriate modeling, and to access significant physical parameters of the medium. The geometry of signal acquisition is no longer linear as in B-mode ultrasound, but circular in the orthogonal plane, with several planar projections at different angles, and based on a multi-channel and multi-frequency device (**Fig.11.2**). USCT provides cross-sectional images of the organ, exploiting the information resulting from the diffraction of the incident acoustic field.

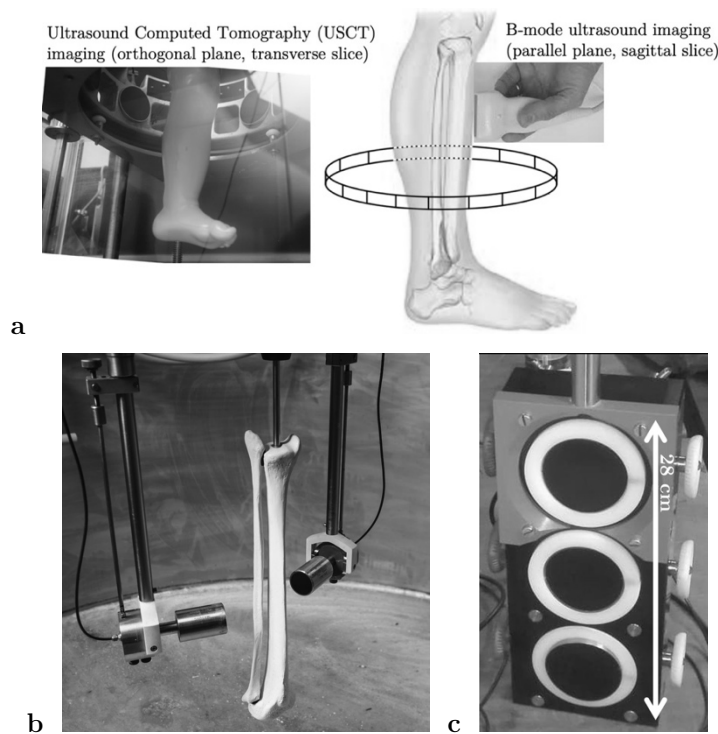


Fig.11.2 a Schematic diagram of B-mode ultrasound and USCT-mode acquisitions. Circular antenna with 8 equally spaced transducers with a child ankle/foot model (SawbonesTM), b 2D-mechanical scanner with a geometrical bone-mimicking phantom (SawboneTM), c 3-frequency linear transducer array

USCT has been steadily improved since the first applications in the mid-1970s, to the development of clinical scanners for breast imaging, providing images with high spatial resolution (André et al. 1995; Duric et al. 2007; J. F. Greenleaf et al. 1975; James F. Greenleaf and Bahn 1981; Hopp et al. 2018; J.-P. Lefebvre, Lasaygues, and Mensah 2009; Mensah and Ferriere 2004; J. W. Wiskin et al. 2017). Whether in wave reflection, transmission or diffraction mode, the mathematical approaches to USCT are adapted when the acoustic impedance contrast between tissues is low. However, these approaches are considered insufficient in the presence of bone whose acoustic impedance is very different from that of the surrounding soft tissues. The solutions for imaging bone with surrounding tissue and marrow consist in optimally integrating the induced non-linear effects, by iterative and adaptive schemes either by keeping the projection-like geometry of Radon and forms of variations of the higher-order Born approximation, or by extending the problem to the full waveform inversion. This chapter presents relevant strategies to adapt USCT to bone imaging, and in particular to the special case of small children’s bones.

11.2. Linear qualitative USCT

The traditional definition of USCT is based on the Radon transform inversion theorem (Devaney 2012; Kak and Slaney 2001). Let us consider a 2D non-circular isotropic elastic cylindrical cavity with generators parallel to the z -axis, immersed in a water-like homogeneous surrounding medium, named the constant background. The canonical geometry is depicted in **Fig.11.3**. In practice, the projections, i.e., the measurements, are made on a circle (2D) Σ surrounding an object D at equal distance from the center of rotation. There is a bijection between the determination of the object in a Euclidean space \mathbb{R}^n and its determination in the associated Radon space $\mathcal{S}: \mathbb{R}^+ \times S^{n-1}$ where $n \in \{1, 2, 3\}$ denotes the dimension of the Euclidean space. A function defined on the Radon space is called a sinogram (all angular projections). A function defined on the Euclidean space is called an image, the elements of the discretized space being pixels (2D) and voxels (3D). In this context, image reconstruction refers to the operation of synthesizing the projections, i.e., transforming the information contained in the sinogram into an image.

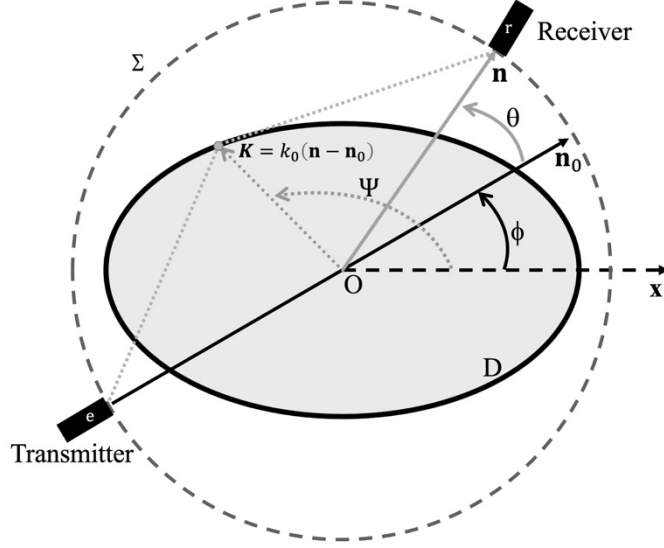


Fig.11.3 Canonical geometry of acquisition

Let us assume that the object D lies in the D space region and is characterized by its space-variable compressibility $\chi(\mathbf{x})$, and the spatial distribution of mass density $\rho(\mathbf{x})$, both independent of time t . Let χ_0 (respectively ρ_0) be the compressibility (respectively the mass density) of the constant background.

The acoustic pressure $p(\mathbf{x}, t)$ is driven by the wave equation:

$$-\frac{1}{c_0^2} \frac{\partial^2 p(\mathbf{x}, t)}{\partial t^2} + \nabla^2 p(\mathbf{x}, t) = \frac{\gamma_\chi(\mathbf{x})}{c_0^2} \frac{\partial^2 p(\mathbf{x}, t)}{\partial t^2} + \nabla \cdot (\gamma_\rho(\mathbf{x}) \nabla p(\mathbf{x}, t)) \quad (11.1)$$

c_0 is the wave velocity in the constant background. $\nabla = \left\langle \frac{\partial}{\partial x}, \frac{\partial}{\partial y}, \frac{\partial}{\partial z} \right\rangle$ is the gradient differential operator. $\gamma_\chi(\mathbf{x})$ is the relative fluctuation of the compressibility, and $\gamma_\rho(\mathbf{x})$ is the relative fluctuation of the mass density:

$$\gamma_\chi(\mathbf{x}) = \frac{\chi(\mathbf{x}) - \chi_0}{\chi_0}, \quad \gamma_\rho(\mathbf{x}) = \frac{\rho(\mathbf{x}) - \rho_0}{\rho_0} \quad (11.2)$$

$\gamma_\chi = \gamma_\rho = 0$ outside D . Let us consider an incident plane wave excitation of pulsation ω , amplitude $P_i^0(\omega)$, direction of incidence \mathbf{n}_0 , and wave number $k_0 = \frac{\omega}{c_0}$ in the background:

$$p_i(\mathbf{x}, t) = P_i^0(\omega) e^{-j(\omega t - k_0 \mathbf{n}_0 \cdot \mathbf{x})} = P_i(\mathbf{x}, \omega) e^{-j\omega t} \quad (11.3)$$

with

$$P_i(\mathbf{x}, \omega) = P_i^0(\omega)e^{jk_0\mathbf{n}_0\cdot\mathbf{x}} \quad (11.4)$$

The solution will be in the form $p = Pe^{-j\omega t}$. Then P is a solution of the Lippman-Schwinger integral equation ($\forall \mathbf{x} \in \mathbb{R}^2$):

$$P(\mathbf{x}, \omega) = P_i(\mathbf{x}, \omega) + \int_D G_0(\mathbf{x}, \mathbf{x}', \omega) \left[-k_0^2 \gamma_\chi(\mathbf{x}')P(\mathbf{x}', \omega) + \nabla \cdot \left(\gamma_\rho(\mathbf{x}') \nabla P(\mathbf{x}', \omega) \right) \right] d^2 \mathbf{x}' \quad (11.5)$$

where G_0 is the 2D-free space Green function:

$$G_0(\mathbf{x}, \mathbf{x}', \omega) = -\frac{j}{4} H_0^{(1)}(k_0 |\mathbf{x} - \mathbf{x}'|) \quad (11.6)$$

$H_0^{(1)}$ is the first Hankel function. The forward problem consists in modeling the total field P and diffracted field P_d ($P_d = P - P_i$) from the incident field and the *a priori* physical parameters of the object:

$$\left(\gamma_\chi, \gamma_\rho \right), P_i \Rightarrow P \quad (11.7)$$

The inverse problem (reconstruction procedure) consists in finding the parameter map from the incident field and the diffracted field measured at several points on Σ :

$$P_i, P_\Sigma \Rightarrow \left(\gamma_\chi, \gamma_\rho \right) \quad (11.8)$$

These measurements satisfy the observation equation. For an object whose acoustic impedance is close to that of the constant background, the diffracted field is weaker than the incident field ($P_d \ll P_i$), and the first-order Born approximation can be used ($\forall \mathbf{y} \in \Sigma$):

$$P_d(\mathbf{y}, \omega) \approx \int_D G_0(\mathbf{y}, \mathbf{x}', \omega) \left[-k_0^2 \gamma_\chi(\mathbf{x}')P_i(\mathbf{x}', \omega) + \nabla \cdot \left(\gamma_\rho(\mathbf{x}') \nabla P_i(\mathbf{x}', \omega) \right) \right] d^2 \mathbf{x}' \quad (11.9)$$

These equations lead to a linear relationship between the physical parameters $(\gamma_\chi, \gamma_\rho)$ and the diffracted field P_d . A method to solve the inverse problem consists in performing a far-field asymptotic development, i.e., great distance with respect to the wavelength and the size of the object ($\forall \mathbf{x}' \in D$):

$$k_0 |\mathbf{y} - \mathbf{x}'| \gg 1, |\mathbf{y}| \gg |\mathbf{x}'| \quad (11.10)$$

so that $|\mathbf{y} - \mathbf{x}'| \approx |\mathbf{y}| - \mathbf{n} \cdot \mathbf{x}'$. $\mathbf{n} = \frac{\mathbf{y}}{|\mathbf{y}|}$ defines the direction of observation, and \mathbf{y} is the position of the receiver. The asymptotic diffracted field is written as follows:

$$P_d(\mathbf{y}, \omega) \approx P_0^i(\omega) \left(\frac{i}{4} \sqrt{\frac{2}{\pi|\mathbf{y}|}} e^{j(k_0|\mathbf{y}| - \frac{\pi}{4})} \right) h(\mathbf{n}_0, \mathbf{n}, \omega) \quad (11.11)$$

$h(\mathbf{n}_0, \mathbf{n}, \omega)$ is the transfer function, or the frequency response, of the diffracting object for directions of incidence \mathbf{n}_0 and observation \mathbf{n} :

$$h(\mathbf{n}_0, \mathbf{n}, \omega) = |k_0|^{3/2} \left[\hat{\gamma}_\chi(\mathbf{K}) + \mathbf{n}_0 \cdot \mathbf{n} \hat{\gamma}_\rho(\mathbf{K}) \right] \Big|_{\mathbf{K}=k_0(\mathbf{n}-\mathbf{n}_0)} \quad (11.12)$$

$\hat{\gamma}_\chi(\mathbf{K})$ and $\hat{\gamma}_\rho(\mathbf{K})$ are the 2D-spatial Fourier transforms of the physical parameters $\gamma_\chi(\mathbf{x})$ and $\gamma_\rho(\mathbf{x})$. The transfer function $h(\mathbf{n}_0, \mathbf{n}, \omega)$ then gives access to the object function, or the contrast function, $O(\mathbf{x}) = [\gamma_\chi(\mathbf{x}) + \mathbf{n}_0 \cdot \mathbf{n} \gamma_\rho(\mathbf{x})]$ with the spectrum $\hat{O}(\mathbf{K})$:

$$h(\mathbf{n}_0, \mathbf{n}, \omega) = \frac{|\mathbf{K}|^{3/2}}{[2(1-\mathbf{n}_0 \cdot \mathbf{n})]^{3/4}} \hat{O}(\mathbf{K}) \Big|_{\mathbf{K}=k_0(\mathbf{n}-\mathbf{n}_0)} \quad (11.13)$$

11.2.1. Qualitative imaging

Instead of directly reconstructing the physical parameters $\gamma_\chi(\mathbf{x})$ and $\gamma_\rho(\mathbf{x})$, the reconstruction will be done on the object function $O(\mathbf{x})$. Because of the derivative, this “object” has a better contrast than the initial physical object. This is qualitative imaging.

With an angular parameterization (ϕ, θ) with respect to the Cartesian coordinates $(0, \mathbf{i}, \mathbf{j})$, where $\phi \equiv (0, \mathbf{i}, \mathbf{n}_0) \in [0, 2\pi]$ is the incidence angle, and $\theta \equiv (\mathbf{n}_0, \mathbf{n}) \in [-\pi, \pi]$ is the diffraction angle (**Fig.11.3**), the transfer function is written as follows, setting $h(\mathbf{n}_0, \mathbf{n}, \omega) \equiv h(\phi, \theta, \omega)$:

$$h(\phi, \theta, \omega) = \left[\frac{K}{2 \sin(\frac{\theta}{2})} \right]^{3/2} \hat{O}(\mathbf{K}) \Big|_{\mathbf{K}=K\xi} \quad (11.14)$$

with $K = 2k_0 \sin(\frac{\theta}{2})$ and ξ is the unit vector such that $(0, \mathbf{i}, \xi) \equiv \Psi = \{\phi + \frac{\theta}{2} - \frac{\pi}{2}\}$, and by inversion:

$$\hat{O}(K, \Psi) = \left[\frac{K}{2\sin(\frac{\theta}{2})} \right]^{\frac{3}{2}} h\left(\Psi - \frac{\theta}{2} + \frac{\pi}{2}, \theta, \frac{Kc_0}{2\sin(\frac{\theta}{2})}\right) \quad (11.15)$$

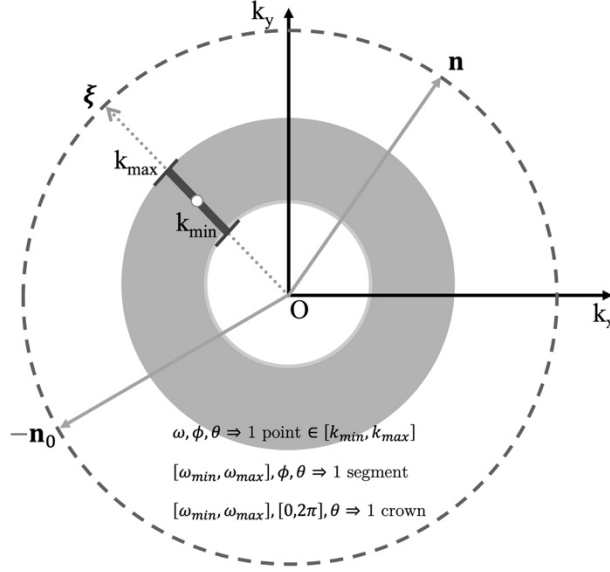


Fig.11.4 Slice-to-slice coverage of the 2D-spatial Fourier domain

All transmitter-receiver configurations have the same bisecting line $(0, \mathbf{i}, \boldsymbol{\xi})$ regardless of the angle θ between the transmitter and the receiver, and give access to a cross-section at the same angle Ψ (**Fig.11.4**). Only the extent of the cross-section varies according to the change in variables $\omega = [\omega_{min}, \omega_{max}]$:

$$K = [K_{min}, K_{max}] = 2\sin\left(\frac{\theta}{2}\right)[k_{min}, k_{max}] \quad (11.16)$$

11.2.2. Reconstruction from radial cross-sections

The inversion process consists in inverting the spatial Fourier transform of the object function:

$$O(\mathbf{x}) = \frac{1}{(2\pi)^2} \int_0^{2\pi} d\Psi \int_0^\infty K \hat{O}(K, \Psi) e^{iK\xi \cdot \mathbf{x}} dK \quad (11.17)$$

This formula corresponds to the reconstruction algorithm by summation of the filtered backprojections (inverse Radon transform):

$$O(\mathbf{x}) \equiv O(x, y) = \frac{1}{2\pi} \int_0^{2\pi} d\Psi P_{\Psi}^F(x\cos\Psi + y\sin\Psi) \quad (11.18)$$

$$P_{\Psi}^F(\xi) = \frac{1}{2\pi} \int_{-\infty}^{\infty} F(\mathbf{K}) P_{\Psi}(\mathbf{K}) e^{j\mathbf{K}\cdot\xi} d\mathbf{K} \quad (11.19)$$

- For a given angle Ψ , $\hat{P}_{\Psi}(\mathbf{K}) = \hat{O}(\mathbf{K}, \Psi)$ is a radial cross-section of the spatial Fourier transform $\hat{O}(\mathbf{K})$ of the object function $O(\mathbf{x})$.
- $P_{\Psi}(\mathbf{x})$ is a projection of the object function $O(\mathbf{x})$ according to the direction ξ of angle $(\mathbf{i}, \xi) \equiv \Psi$ (slice-projection theorem (Deans 2007)).
- $P_{\Psi}^F(\xi)$ is a projection $P_{\Psi}(\mathbf{x})$, filtered by the filter F , with the frequency response $\hat{F}(\mathbf{K}) = |\mathbf{K}|$.
- $P_{\Psi}^F(x\cos\Psi + y\sin\Psi)$ is the backprojection of the filtered projection in the direction orthogonal to the ξ -direction.

For N equiangularly distributed projections over $[0, 2\pi]$, the discrete version of the reconstruction algorithm is written as follows:

$$O(\mathbf{x}) \equiv O(x, y) = \frac{1}{2N} \sum_{n=0}^{N-1} P_n^F(x\cos\Psi_n + y\sin\Psi_n) \quad (11.20)$$

11.2.3. Elliptical kernel

The far-field hypothesis (11.10) has limitations in near-field USCT, e.g., probe close to the organ. When the incident field is modeled by a spherical wave emitted at a source point e , by composition of Green's functions, the projections of the imaged object are ellipses. This is called spherical wave analysis of the object, as opposed to the plane wave analysis described above. The inversion problem for a set of receivers r is identified with the inversion of an elliptical spectrum. The inversion algorithm developed in particular by Mensah *et al.* (Mensah and Ferriere 2002; Franceschini et al. 2007) is analogous to filtered backpropagation but the backprojections are made on ellipses (Σ_t) of focus (\mathbf{x}, r) defined by $c_0 t = |\mathbf{r} - \mathbf{x}| + |\mathbf{x} - e|$. This method gives qualitative images allowing a significant gain in resolution (P. Lasaygues et al. 2002; Rouyer, Lasaygues, and Mensah 2012).

11.2.4. Acoustic and elastic object functions

In the general case the reconstructed object is the object or contrast function $O(\mathbf{x})$ which can be evaluated as a function of the diffraction angle θ , and of the acoustic or elastic physical parameters. Considering a fluid medium, the object function is written as follows:

$$O(\mathbf{x}) = [\gamma_Z(\mathbf{x}) + \cos\theta \gamma_\rho(\mathbf{x})] \quad (11. 21)$$

or

$$O(\mathbf{x}) = [(1 - \cos\theta) \gamma_Z(\mathbf{x}) + (1 + \cos\theta) \gamma_c(\mathbf{x})] \quad (11. 22)$$

with $\gamma_Z(\mathbf{x})$ (respectively $\gamma_c(\mathbf{x})$) the relative fluctuation of the acoustic impedance $Z(\mathbf{x}) = \sqrt{\frac{\rho(\mathbf{x})}{\chi(\mathbf{x})}}$, (respectively the acoustic wave velocities $c(\mathbf{x})$):

$$\gamma_Z(\mathbf{x}) = \frac{Z(\mathbf{x}) - Z_0}{Z_0}, \gamma_c(\mathbf{x}) = \frac{c(\mathbf{x}) - c_0}{c_0} \quad (11. 23)$$

In the case of an isotropic solid elastic medium, the function is written as follows:

$$O(\mathbf{x}) = [\gamma_\lambda(\mathbf{x}) - \cos\theta \gamma_\mu(\mathbf{x}) + 2\cos\theta \gamma_\rho(\mathbf{x})] \quad (11. 24)$$

with

$$\gamma_\lambda(\mathbf{x}) = \frac{\lambda(\mathbf{x})}{\lambda_0 + 2\mu_0}, \gamma_\mu(\mathbf{x}) = \frac{\mu(\mathbf{x})}{\lambda_0 + 2\mu_0} \quad (11. 25)$$

and λ, μ , are the space-variable Lamé coefficients.

These equalities show that the diffracted field by each type of inhomogeneity has a specific directivity pattern that can be separated according to the type of spatial scan performed: transmission ($\theta = 0^\circ$), reflection ($\theta = 180^\circ$), or diffraction ($\forall\theta$) (**Fig.11.5**).

In the pure reflection-mode USCT (similar to a circular B-mode ultrasound imaging) ($\theta = 180^\circ$), the transfer function becomes:

$$h(\omega) = -k_0^2 \hat{\gamma}_Z(\mathbf{K}) \text{ with } \mathbf{K} = -2k\mathbf{n}_0 \quad (11. 26)$$

with $\hat{\gamma}_Z$ the 2D-spatial Fourier transform of γ_Z . In the pure transmission-mode USCT ($\theta = 0^\circ$), the transfer function becomes:

$$h(\omega) = -k_0^2 \hat{\gamma}_c(\mathbf{K}) \quad (11. 27)$$

with $\hat{\gamma}_c$ the 2D-spatial Fourier transform of γ_c . These formulas show that the relative fluctuation of the acoustic impedance (respectively of the acoustic wave velocities) can be expected from reflection measurements (respectively from transmission measurements) (J.-P. Lefebvre, Lasaygues, and Mensah 2009).

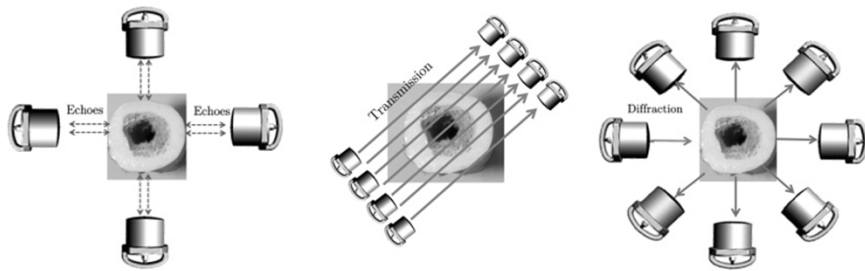


Fig.11.5 Reflection-mode USCT (**left**), transmission-mode USCT (**center**) and diffraction-mode USCT (**right**)

11.2.5. Hard biological tissue imaging

Difficulties arise in the presence of bone because of the large differences in acoustic impedance between soft tissues, including marrow, represented by the constant water-like background, and bone. Propagation disturbances affect the signals and bias the imaging process, decreasing the contrast-to-noise ratio (CNR). The weak scattering hypothesis (11.9) is not realistic. Physical phenomena can be divided into 2 classes. In the first class, the phenomena are related to the reflection and transmission of waves at the boundaries of the bone. These phenomena include the attenuation of waves. The second-class phenomena are related to the spatial dependence of the velocity of the transmitted waves since they will be accelerated into the bone, and it is necessary to take into account a temporal correction factor. It thus becomes necessary to change the methods used for the acquisition and the processing of the ultrasonic signals, and finally to adapt the inversion schemes to non-linear formalisms.

Nevertheless, if the imaging objective involves morphometrical parameters such as the bone thickness, the problem can be viewed as how to identify a water-like cavity (the object) located in an elastic cylinder immersed in a

water-like fluid. Numerical modeling shows that the Born approximation would still be satisfied if the phase shift introduced by the heterogeneity is less than π (Delamare, Lefebvre, and Lasaygues 1997; Kak and Slaney 2001; J. P. Lefebvre et al. 2002). The validity of the hypothesis depends on the size (versus wavelength) of the inhomogeneity and the impedance contrast (Kak and Slaney 2001). Thus, one solution consists in using the low-frequency (≤ 3 MHz) ultrasonic wave propagation scheme. In this case, the background can be defined in terms of the solid part without any hole and surrounded by water, and the perturbation, i.e., the object to be reconstructed, would be the cavity. Image reconstruction can then be performed by the previous backprojection algorithm implemented with standard graphics algorithms (P. Lasaygues, Lefebvre, and Mensah 1997; Philippe Lasaygues 2006). The earliest work on this approach dates back to the 1980s (Carson 1977; André et al. 1980; Sehgal et al. 1988). In the 1990s, other teams proposed solutions to take into account some of the refraction effects, or by combining several B-mode ultrasound angular scans. (Migeon et al. 1998; Detti, Kourtiche, and Nadi 2002). To illustrate the interest of the linear morphometrical USCT, we tested the algorithm on a geometrical bone-mimicking phantom (tibia-fibula, without soft tissues) (SawbonesTM), and one *ex vivo* chicken drumstick. The details of the protocols and algorithms used can be found in (Philippe Lasaygues 2006; Philippe Lasaygues et al. 2017). The cavity diameter of the tibia phantom was of 12.5 mm, and the overall length of 42 cm, and the solid fibula had no inner cavity. The distance between bones was measured at ~ 8 mm using a caliper. USCT images of objects were compared with X-ray scan (μ -CT scanners, nanoScan[®] MedisoTM, Hungary, for the SawbonesTM sample, and EasyTom XL 150[®] RX SolutionsTM, France, for the chicken drumstick). The slice thickness of the X-ray cross-section was 50 μ m and the number of projections was 360. Cross-sections were chosen in the cortical areas of the bones; 100 mm from the proximal epiphysis for the bone phantom; and 25 mm for the chicken drumstick. **Fig.11.6** shows the image of the SawbonesTM phantom obtained by diffraction-mode tomography with 8 dual-frequency transducers, 1 MHz and 2.25 MHz, respectively (32 equally spaced rotations, 256 x 256 signals) (Philippe Lasaygues et al. 2018). **Fig.11.7** shows the image of the *ex vivo* chicken drumstick obtained at the three frequencies (500 kHz, 1 MHz & 2.25 MHz) in reflection mode (720 backprojections, 511 x 511 pixels).

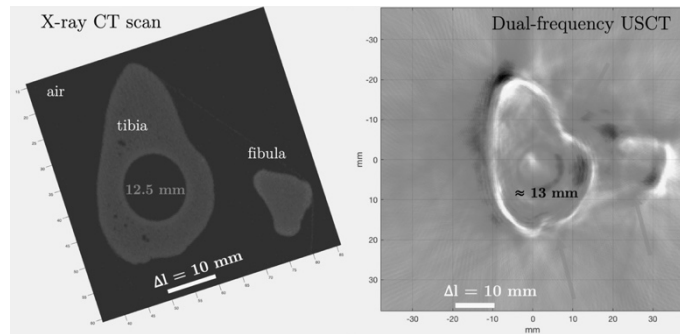


Fig.11.6 Geometrical bone-mimicking phantom (Sawbone™), X-ray tomography (478 x 478 pixels) (courtesy of CERIMED, France) (**left**), Dual-frequency (1 MHz & 2.25 MHz) diffraction-mode USCT (256 x 256 signals, 255 x 255 pixels) (**right**) (Philippe Lasaygues et al. 2018)

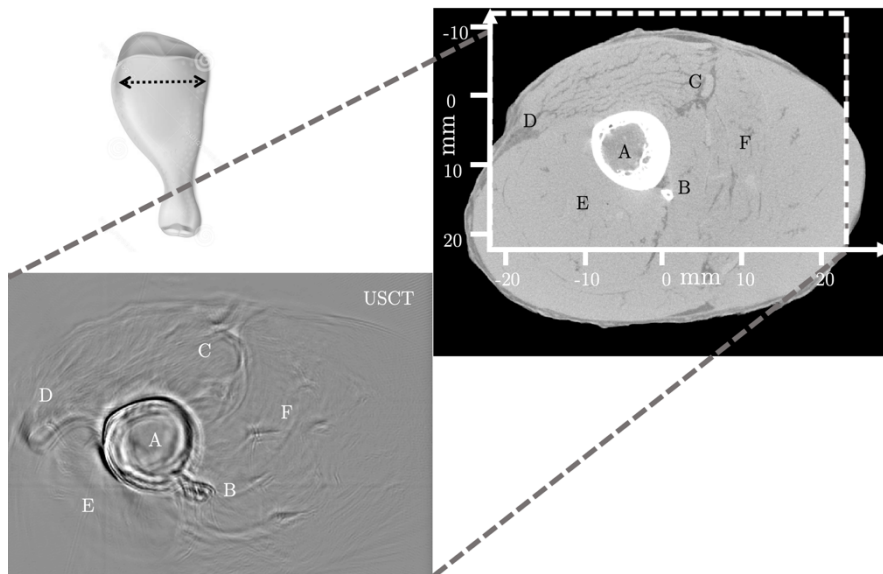


Fig.11.7 *Ex vivo* chicken drumstick, 3-frequency reflection-mode USCT (500 kHz, 1 MHz & 2.25 MHz, 720 backprojections, 511 x 511 pixels) [**A** Tibia, **B** Fibula, with marrow, **C-D** Muscle fixed on the kneecap with linear long fibers, **E** Dense fat accumulation, **F** Fibrous muscle and fat tissue] (**left**), X-ray tomography (600 x 600 pixels, resolution 50 μm) (courtesy of the Fédération de Recherche Fabri de Peiresc, Marseille, France) (**right**)

11.2.6. Adapted signal processing

The use of low frequencies thus provides an effective possible solution. However, if the depth of the field increases, the resolution of the signals, and hence that of the reconstructed images, is bound to decrease. Even with low frequencies, the wave propagation process generates extremely complex acoustic signals consisting of several packets with different signatures, which is often difficult to analyze in terms of the wave paths, volume, guided or surface waves, and attenuation, and to interpret. It is therefore interesting to focus on signal processing. Our group has developed a procedure of multi-scale decomposition of the signals, adapted to the USCT process (Zheng and Lasaygues 2013) and making it possible to process all the wave packets available in terms of frequency and time (Loosvelt and Lasaygues 2011). This method, called the “Wavelet-based Coded-Excitation” (WCE) method, can be used to determine, independently, the velocity of the ultrasonic wave and the wave path across the thickness of the cortical bone area geometrically assimilated to a succession of contiguous parallelepiped plates (**Fig.11.8**). The method can also be adapted to the apparent bone mass density measurement (Metwally et al. 2015). When it was adapted to the diffraction-mode USCT (Philippe Lasaygues et al. 2017), the method improved the CNR by at least 11% (**Fig.11.6**).

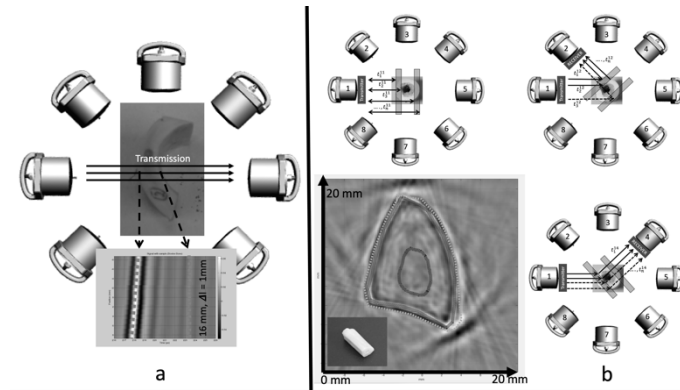


Fig.11.8 **a** Measurement of the thickness of a cortical bovine bone section using the WCE method in transmission mode, **b** The transmission-echo mode USCT of a fresh child fibula (Zheng and Lasaygues 2013) [The cortical bone boundaries are plotted using an automatic "Snake" algorithm (clear dotted outer boundary), and using an algorithm based on the adapted WCE-method (two inner limits in gray lines)]

11.2.7. Adapted image processing

Although pre-processing can be an interesting solution, it is also relevant to study the post-processing of the images to try to further improve the CNR, and to develop tools for morphometric measurements. The automatic segmentation of images is a widespread problem, especially in the field of medical imaging, when, because of the inhomogeneity and complexity of the anatomical topology, there is a tendency towards image degradation (Dera, Bouaynaya, and Fathallah-Shaykh 2016). In the last two decades, a flurry of research has involved the use of a deep learning process for image processing, such as the use of the 2D wavelet-based algorithms for image denoising because of the energy compaction and multiresolution properties of wavelet decomposition (Hongqiao and Shengqian 2009; Mayer et al. 2012). Our group has first proposed simple methods such as the “Snake” algorithm (**Fig.11.8**) (Philippe Lasaygues 2006), or statistical methods (Malagon Torres et al. 2019), then more powerful and automatic methods based on wavelet decomposition such as the Haar wavelet 2D-decomposition (Mallat and Hwang 1992). As shown in **Fig.11.9**, this method allows the denoising of the USCT image and a segmentation of the contours of the object (Fradi et al. 2018). Deep learning methods are increasingly used in medical ultrasonic imaging. In the case of bone tissue, we have proposed an automatic structure identification procedure using combining k -means (Jose, Ravi, and Sambath 2014) and *Ostu* algorithms (Liu 2011). **Fig.11.10** shows an example of binarization of a USCT image, and the detection of three artificial defects of increasing size (Fradi, Lasaygues, and Machhout 2019).

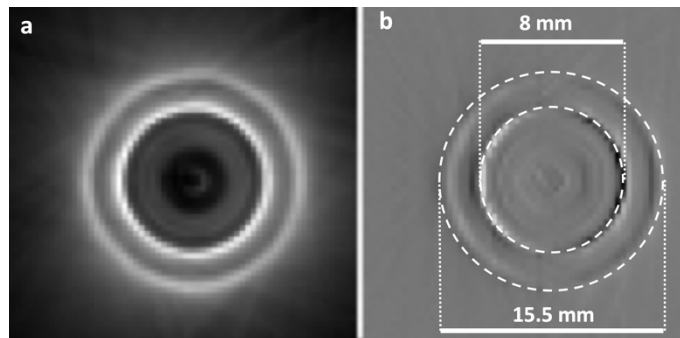


Fig.11.9 Haar wavelet-based processing algorithm to automatically detect the external and internal boundaries (dotted circles) of a circular cylindrical Perspex tube, **a** Initial diffraction-mode USCT, **b** Image after denoising with automatically detected contours [*radius measurements after processing vs. with a calipers, $R_{ext} = 7.75$ mm*]

vs. 8 mm, $R_{int} = 4 \text{ mm vs. } 4.3 \text{ mm}$] (Marwa et al. 2019), Copyright (2021) with permission from SPIE Publishing

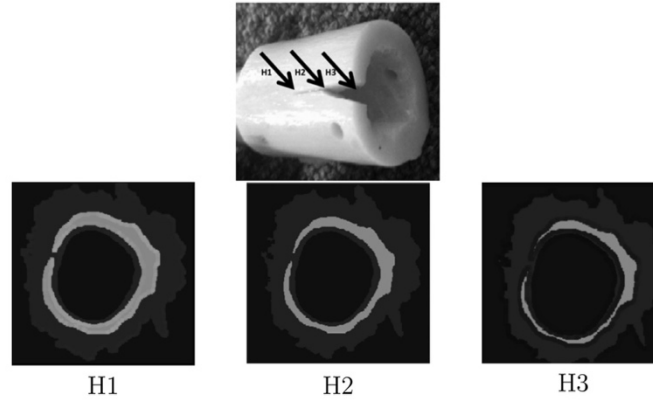


Fig.11.10 Diffraction-mode USCT binarization and cortical human femur defect identification for 3 different heights (H1, H2 and H3), using deep learning processing based on the k-means and Ostu algorithms (Marwa et al. 2019), Copyright (2021) with permission from SPIE Publishing

11.2.8. Precision analysis for 2D inverse scattering

One of the main key points in 2D inverse scattering is the quantitative prediction of the expected precision of the reconstructions. In other words, the challenge for imaging systems is to determine the configuration of measurements necessary to achieve satisfactory performance and resolution. Naturally, one always searches for the best precision, while keeping the instrument as simple as possible. It is thus of interest to be able to predict beforehand the precision of a given apparatus before effectively constructing it. But how to define the criterion of satisfaction? One way to answer this problem is to quantify the amount of information available in the measurement data in view of the physical parameters to be reconstructed. In the framework of the estimation theory, the system performance can be analyzed based on the measurement model and the available *a priori* knowledge. The reconstruction error can be directly used as a decreasing function of the amount of information available. This error depends not only on the inversion algorithm used but also on the object to be reconstructed. Taking into account the randomness of the measurements implies the use of

numerical simulation methods such as Monte-Carlo methods to calculate the error (Diong et al. 2015). In diffraction-mode USCT, this approach is quite costly in terms of computation time. A second solution consists in using estimation performance bounds, and statistical processing of the information. The performance bounds make it possible to analyze the optimal precision of the estimates for the different physical models considered, without being influenced by the choice of the estimation method. They thus constitute an interesting alternative to the optimization of an imaging system according to the class of objects considered. Our group has analyzed the precision of the impedance contrast estimators with the Cramer-Rao Bound (CRB) assuming an additive complex circular Gaussian noise at the receivers (Diong et al. 2016). An adapted framework was derived to handle acoustic imaging configuration. Firstly, we took advantage of the CRB to derive some design guidelines when selecting the parameters of the “optimal” experimental configuration. Secondly, we tried to appraise the effect of the error model when a classical linear approximation, such as the Born approximation, is selected and when it is not (**Fig.11.11**).

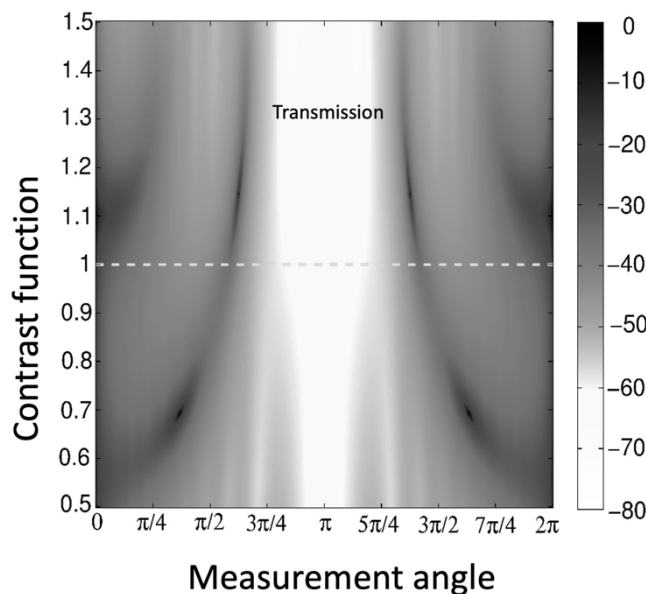


Fig.11.11 Impact of the measurement angle on the Cramer-Rao bound for the object function γ_{χ} under Born approximation, and a known object radius, [radius of the circle $\Sigma = 5\lambda$, surrounding an object D of a radius = 0.5λ (λ : wavelength)]

11.3. Non-linear quantitative USCT

In the context of linear USCT, the fluid-like modeling thus fails to provide quantitative information about the physical parameters of bone tissues. For certain configurations, e.g., in the case of adjacent bones, the phenomena described above affect the signals received so much that an inversion done under the hypothesis of a fluid medium introduces important artefacts. Recently, J. Wiskin *et al.*, (James W. Wiskin et al. 2019) worked on a complete knee organ (skin, muscles and bone) using a quantitative combined reflection/transmission-mode USCT algorithm. Because of the redundancy of the data and the 3D nature of the reconstruction algorithm, the quantitative accuracy for soft tissues that are closely juxtaposed with the bone is very relevant. The resolution of the resulting images is comparable to that of an MRI image. Nevertheless, the images do not seem to correctly quantify the velocity of waves in the bone. Inaccuracies are due to the mathematical approach involved, which does not take into account shear waves. This is appropriate for an anatomical reconstruction of the bone, but for the identification of its elastic properties shear waves are needed. The problem is thus complex. It can be addressed by suitable nonlinear iterative inversion strategies, either keeping the projection-like geometry of Radon and the high-order Born approximations, or by introducing canonical models, or by implementing the complete waveform inversion without any *a priori* information on the media.

11.3.1. Compound-mode USCT

The first step to avoid including shear waves in the model was to adapt the acquisition protocol. Our group proposed first the Compound-mode USCT to geometrically combine reflection- and transmission-mode acquisitions. Experimentally, this approach is comparable to the non-linear Distorted Born Iterative Method (discussed below) adapted to a bone sample considered as a tube-like sample (Philippe Lasaygues et al. 2005). The solutions are iteratively determined using an inhomogeneous Green function of the background, i.e., the set consisting of the homogeneous solid circular cylinder and the surrounding homogeneous fluid medium, adapted for every iteration. The refraction effects are canceled using a specific set-up in order to correct the temporal bias $\tau(\mathbf{r}, \mathbf{e}, \mathbf{x})$ and to impose straight-line propagation inside the shell of the tube/bone (**Fig.11.12**):

$$\tau(r, e, \mathbf{x}) = \frac{1}{c_0} \int_{e\mathbf{x}+\mathbf{x}r} \frac{c(\mathbf{x}')-c_0}{c_0} d\mathbf{x}' \quad (11.28)$$

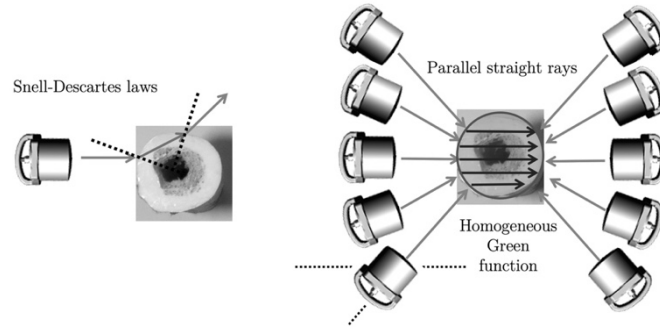


Fig.11.12 Quantitative iterative Compound-mode USCT, Refraction effects according to the Snell-Descartes laws (**left**), Geometrical corrections of the acquisitions to impose straight-line propagation inside the shell of the bone (**right**)

Hence the overall correction is the sum of the respective temporal corrections along the emitter path ($e\mathbf{x}$, located at e) and along the receiver path ($\mathbf{x}r$). Via the iterative procedure, the dimension of the *intercepting* circular cylinder is adapted to the external shape of the bone, measured in echo mode. The unknown wave velocity $c(\mathbf{x})$ is initialized on the basis of prior information which may for instance correspond to the bone average velocity for a patient of equivalent age and health status. Despite limitations due to heavy data processing requirements (even though the WCE method is not added) and complex acoustic signals resulting from the multiple physical effects involved (various paths inside the shell, roughness of the water/bone interfaces), this approach yields correct estimates of the size and shape of the bone and correct identification of the compression wave velocities in a cross-section of a cortical shell. **Fig.11.13** shows the Compound-mode USCT of a human femoral diaphysis with an external diameter of about 32 ± 5 mm and an internal diameter of 16 ± 2 mm. The initial velocity of the compression wave propagating in the bone was set at $3400 \text{ m}\cdot\text{s}^{-1}$. The error remained within reasonable limits of about 7% (Philippe Lasaygues et al. 2005; Ouedraogo et al. 2002). More recently, the Langton group has proposed, as an extension of this compounding approach, a two-component model of the cortical shell to accurately calculate the wave velocity and the thickness (Shortell et al. 2017). Despite promising results, these approaches still remain incompatible with an automatic process involving a large number of data, and thus still difficult to exploit in a clinical field.

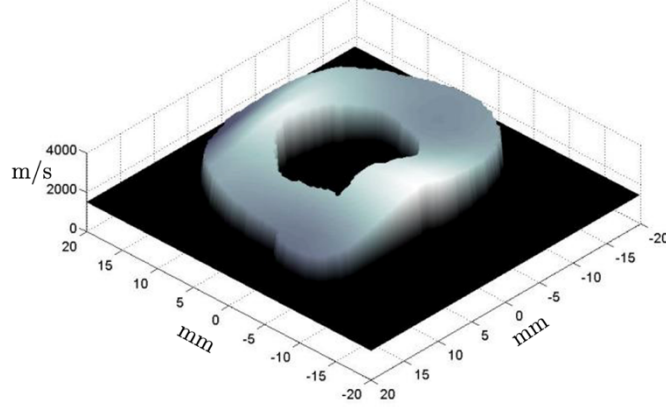


Fig.11.13 Compound-mode USCT (90 angles, 128 translations, 256 x 256 pixels) of a human femur using linear inversion algorithm and adapted experimental Distorted Born Iterative Method [*3D mapping of compression wave velocity (m/s) vs. morphology (mm)*]

To go further, the non-linear and iterative inversion schemes must integrate compression and shear waves. As for the linear scheme, the inverse diffraction problem is defined as the solution of the Lippmann-Schwinger integral equation (11.5), with the need to know the total field $\mathbf{P}(\mathbf{x}, \omega)$ within the region of interest (ROI) containing the object \mathbf{D} (i.e., water/(bone and marrow), or (water and bone)/marrow). The forward problem is defined as the iterative (m) solutions of the Lippmann-Schwinger integral equation (11.5) for the total field:

$$\mathbf{y} \in \Sigma, P_d(\mathbf{y}, \omega) - \hat{P}_d^m(\mathbf{y}, \omega) \approx -k_0^2 \int_D G^m(\mathbf{y}, \mathbf{x}', \omega) \Delta O(\mathbf{x}') P^m(\mathbf{x}', \omega) d^2 \mathbf{x}' \quad (11.29)$$

The medium is then modeled without any *a priori* knowledge, and contrary to what occurs with the experimental Compound-mode USCT, these approaches require only one set of recorded signals. Iterative non-linear algorithms alternate between incrementing the estimate of the object function ($\Delta O(\mathbf{x}) = O(\mathbf{x}) - O_{m-1}(\mathbf{x})$), of the total field P^m and of the Green function G^m . The set of physical parameters of the medium to be imaged, identified by the object function $O(\mathbf{x})$ is obtained by minimizing the difference between the diffracted field recorded at N receivers' positions (\mathbf{r}) and for a single source (\mathbf{e}) ($\mathbf{P}_{\text{mea}}^n(\mathbf{t})$, $n = 1, \dots, N$) and the corresponding numerically modeled field ($\mathbf{P}_{\text{num}}^n$)(**Fig.11.14**).

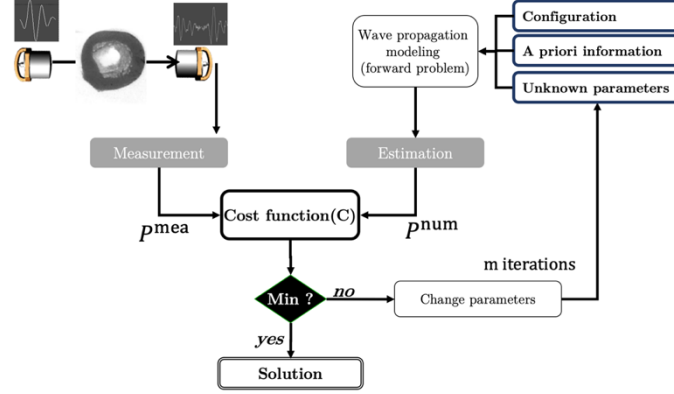


Fig.11.14 Non-linear and iterative adaptive scheme for USCT

The quadratic error or cost function $C(O)$ to minimize writes as follows:

$$C(O) = \sum_n \int [P'_{num}(t) - P'_{mea}(t, O)]^2 dt \quad (11.30)$$

The main common difficulties encountered in the minimization of $C(O)$ are its significant non-linearity with respect to O , the presence of numerous local minima in which the iterative resolution system may remain trapped, and a large number of parameters. An iterative method based on the calculation of the gradient of the cost function is generally chosen to minimize $C(O)$.

11.3.2. Intercepting Canonical Body Approximation (ICBA)

Our group has thus first proposed an extension of the Compound-mode USCT, by which the forward problem was analytically solved using the Intercepting Canonical Body Approximation method (Scotti and Wirgin 1995). For example, the diaphysis of a long bone can be approximated by two *canonical* homogeneous, circular, and concentric cylinders. In this approach, the modeling of the medium was nonetheless based on *a priori* knowledge because the physical parameters (velocities and mass density in this case) and the dimension of the *intercepting* circular cylinders were adapted at each position of the transmitter and the receiver, according to initially known values.

Fig.11.15 shows a comparison of the reconstruction using the first-order Born USCT and the ICBA. The object was a Perspex circular tube, and the data were experimentally collected in diffraction mode. For the dimensions, the method, which is fairly simple to compute, gave very precise results (error less

than a few percent). For the physical parameters (**Fig.11.16**) such as the mass density or the elastic wave velocities, the problem was more complex, and the error increased up to more than 1% (Philippe Lasaygues and Le Marrec 2008).

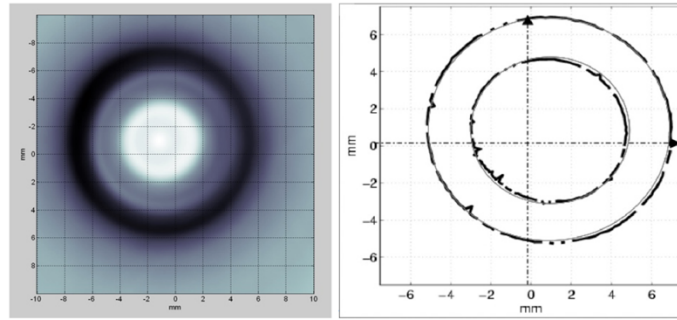


Fig.11.15 Comparison of the experimental reconstruction based on the first-order Born USCT (**left**) and the Intercepting Canonical Body Approximation (ICBA) (**right**) for a Perspex circular tube [*radius measurements with ICBA method vs. calipers*, $R_{ext} = 5.9 \pm 0.5 \text{ mm}$ vs. 6 mm , $R_{int} = 3.8 \pm 0.25 \text{ mm}$ vs. 4 mm] (Philippe Lasaygues and Le Marrec 2008)

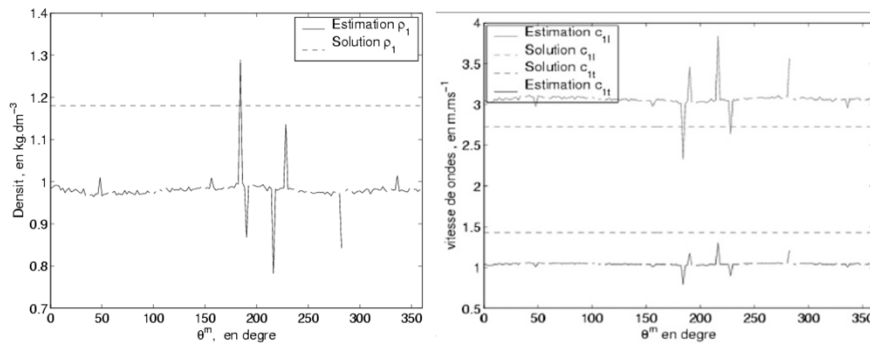


Fig.11.16 Parametric inversion using the Intercepting Canonical Body Approximation (ICBA) in the case of the Perspex circular tube (experimental measurements), Mass densities [$\rho = 1180 \text{ kg/m}^3$] (**left**), Compression (**top right**) [$c_{1l} = 2730 \text{ m/s}$] and shear (**bottom right**) [$c_{1t} = 1430 \text{ m/s}$] wave velocities (Philippe Lasaygues and Le Marrec 2008)

11.3.3. Full-Waveform Inversion (FWI) algorithms

Making assumptions about the object somehow introduces a bias. The objective must therefore be global schemes without any *a priori* knowledge of the medium. Adapted iterative global approaches have been proposed such as the Distorted Born Iterative Method based on high-order Born approximations (Chew 1995; Lu et al. 1996; Osama S. Haddadin and Ebbini 1997; O.S. Haddadin and Ebbini 1998) or the Contrast Source Method (Berg and Kleinman 1997). Experimental studies have been published in the Electromagnetics domain (Lobel et al. 1996; Tijhuis et al. 2001; Crocco and Isernia 2001; Duchêne 2001; Belkebir and Saillard 2004; Litman and Crocco 2009), but few ultrasonic experimental results are available (Lu et al. 1996; Philippe Lasaygues, Guillermin, and Lefebvre 2006; R. Lavarello and Oelze 2008; R. J. Lavarello and Oelze 2009; Guillermin et al. 2013). More recently, Salehi et al. have developed a mathematical similar framework for an iterative algorithm based on the Kaczmarz method (Salehi 2017). The idea is to calculate the locally adjoint operator for a hole inside a cortical tube. Belanger et al. have adapted a “*hybrid algorithm for robust breast ultrasound tomography*” (HARBUT) for the velocity mapping of the cortical bone (Falardeau and Belanger 2018). These last two algorithms have been tested on numerical and experimental data on bone-mimicking phantom and the results are very encouraging. Although artefacts were present in the images generated, the results obtained made it possible to discriminate between a healthy bone phantom and a pathological one based on measurements of the cortical bone thickness and of the average velocity of the ultrasonic waves.

In our first approach, a mean-square solution was calculated using the Polak-Ribière conjugate-gradient method to minimize $\mathbf{C}(\mathbf{O})$, associated with a Tikhonov regularization process. The detail of the algorithm is presented in (Philippe Lasaygues, Guillermin, and Lefebvre 2006; Guillermin et al. 2013; Guillermin, Lasaygues, and Rabau 2015). In the inversion algorithm proposed, Green’s theorem is used to obtain a time-domain integral representation of the diffracted field. A discrete formulation of the integral representation is obtained by replacing the object to be imaged by an array of identical square cells. Each of which is small enough to assume that the object function $\mathbf{O}(\mathbf{x})$ and the total field \mathbf{P} are constant inside it. However, in this first algorithm, the forward problem modeling assumes constant tissue mass density and high shear wave attenuation. The second algorithm we proposed consists in importing the most sophisticated techniques for a large amount of data, these techniques being at the forefront in the field of geophysics. The

method proposed uses the “full-waveform inversion” (FWI) technique, based on a full numerical modeling of wave propagation in the medium. The term “full” refers to the fact that the full-time series are used. The detail of the algorithm is presented in (Bernard et al. 2017; Espinosa et al. 2021). The mean-square solution is calculated using the quasi-Newton technique, which uses information based on second-order derivatives in order to accelerate convergence. Both approaches make it possible to converge to the minimum of the function in a larger or smaller number of iterations, depending on the method used and on the complexity of the problem. Nevertheless, the gradient of $C(\mathbf{O})$, that is, its partial derivatives with respect to each element of $\mathbf{O}(\mathbf{x})$, cannot easily be calculated based on a standard and simple finite-difference approach because this would require performing as many forward calculations of wave propagation as the number of parameters, and this for each iteration of the minimization algorithm. In the FWI approach, the adjoining field method, introduced in Seismics in the 1970s (Bamberger et al. 1982), makes it possible to overcome this difficulty. It can be shown that the gradient of the cost function can be obtained as the convolution product of the forward field with an adjoint field obtained by calculating the propagation of the time-reversed residuals:

$$r_n(t) = [P_{mea}^n(-t) - P_{num}^n(-t, \mathbf{O})] \quad (11.31)$$

with each receiver acting as a source. The calculations for two phenomena of wave propagation in the medium are then sufficient to obtain the gradient (in the case of multiple sources, two calculations per source are needed).

The other important difficulty related to the strong non-linearity of $C(\mathbf{O})$ is that gradient-based minimization algorithms only converge to the solution if they are started close to the global minimum, which assumes an initial low bias model. This is rarely the case. For bone imaging, we can exploit the linear USCT which provides a good geometric resolution of external contours. But this is the only unbiased information available. Measurements of the inner (marrow) area or of the compression wave velocity that can be used as *a priori* information are biased because of the fluid modeling used. Imaging of anatomical sites will also require to take into account the surrounding soft tissues. This requires a general resolution of the inverse problem, and the global minimum must be totally unknown. There is nevertheless a risk of remaining trapped in a local minimum. In particular, if there is a difference in propagation time greater than half a period between the computed and real data, the algorithm will attempt to match different cycles of the signals and will not be able to converge (a problem known as “cycle skipping” (Virieux and Operto 2009)). A method to reduce this risk is to use the incremental frequency-hopping approach: first, a low-pass filter is used to retain only the

lowest frequencies and then, once a minimum is obtained, the maximum frequency is slightly increased and the process is run again until all the frequency information is included.

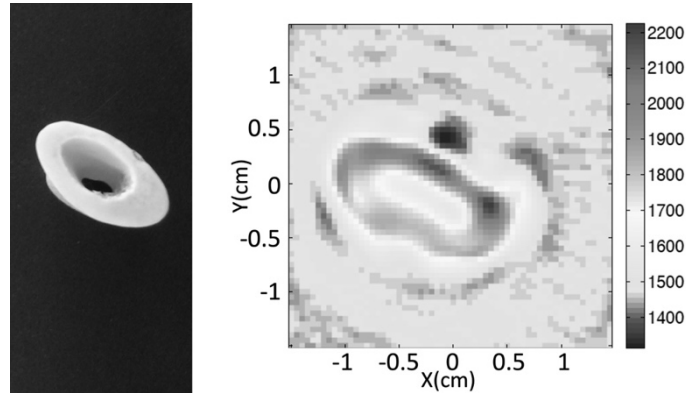


Fig.11.17 Parametric (compression wave velocities) diffraction-mode USCT (64 x 64 pixels) of a fresh lamb shoulder bone using the frequency-hopping and Polak-Ribière conjugate-gradient methods (Guillermin, Lasaygues, and Rabau 2015)

Fig.11.17 shows the experimental result obtained for a fresh and clean lamb shoulder bone using the frequency-hopping and Polak-Ribière conjugate-gradient methods. The usable bandwidth ranged from approximately 150 kHz to 750 kHz. Shear waves in the sample were assumed to be attenuated, and the mass density was assumed to be constant and equal to that of the surrounding water ($\gamma_\rho \rightarrow 0$). Regarding the quantitative aspects, the compression wave velocity was reconstructed with a relative error of about 30% related to the reference measurement, which was 2700 ± 200 m/s. **Fig.11.18** shows the main quantitative (compression wave velocity and mass density) reconstruction obtained with a numerical phantom. The phantom had a realistic geometry of a tibia/fibula adjacent bone, surrounded by a water-like medium. The incident signal was a Ricker (second derivative of a Gaussian) 200 kHz-wavelet, and the virtual 9 cm radius array had 8 sources and 128 receivers. **Fig.11.19** shows non-linear USCT reconstructions for two 20 cm long wax bars with square cross-section (16 mm x 16 mm). Included in one of the targets and located at its center was a 5 mm circular cavity. The compression (respectively, shear) wave velocity was 2050 m/s (respectively, 750 m/s), and the attenuation was 55 Np/m/MHz and (respectively, 650 Np/m/MHz). The wax mass density was 900 kg/m^3 .

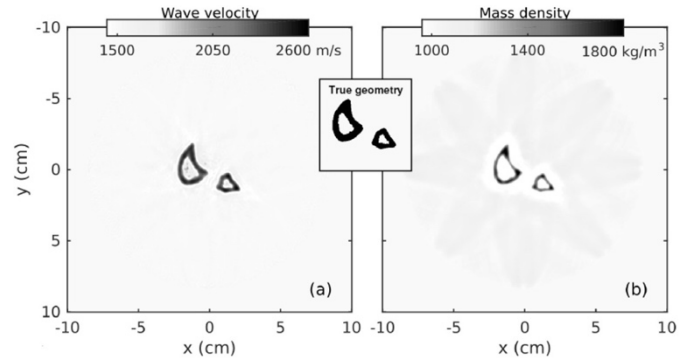
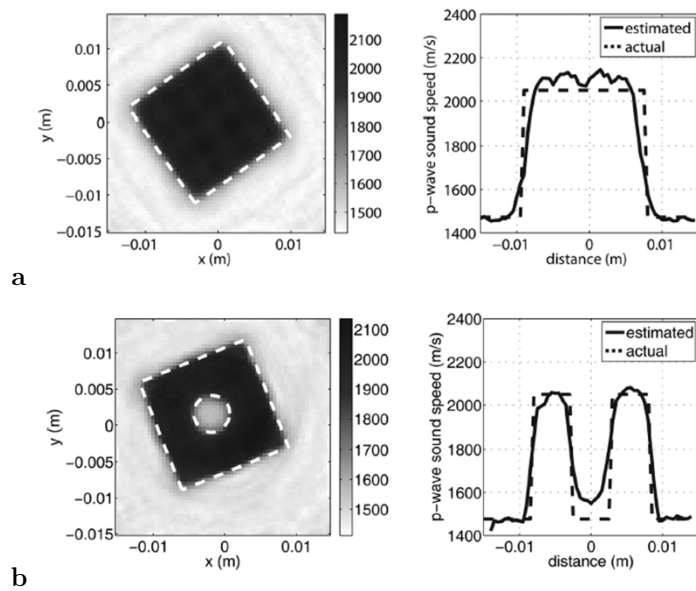


Fig.11.18 Numerical quantitative USCT of a tibia/fibula adjacent bone using the non-linear full waveform inversion method. Images and details can be found in (Bernard et al. 2017), Copyright (2021) with permission from IOP Publishing



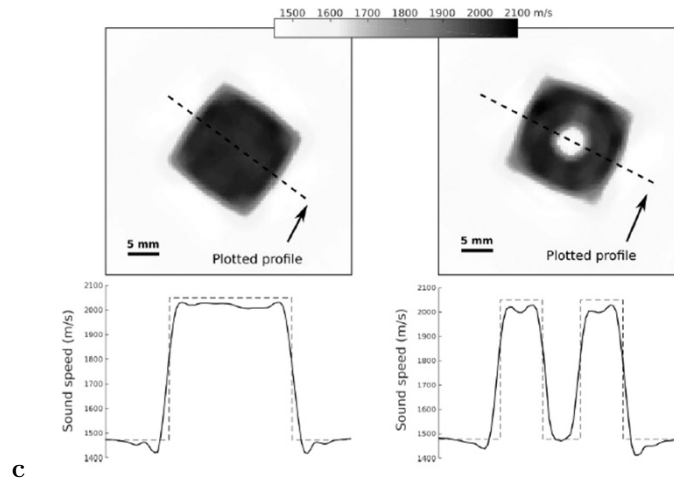


Fig.11.19 Ultrasound Computed Tomography based on non-linear inversion schemes for wax targets, without and with a hole (experimental data), **a-b** The frequency-hopping and Polak-Ribière conjugate-gradient methods), Reproduced from Guillermín et al. 2013, with the permission of the Acoustical Society of America, **c** The full waveform inversion and Quasi-Newton method (Espinosa et al. 2021)

When it can be made to work, non-linear USCT offers significantly-improved resolution compared with simpler methods based for example on travel times only or on a linearization of propagation in the medium (Born approximation), at the price of a higher calculation cost. But the computational cost issue tends to be less limiting nowadays, thanks to the continuous increase in the power of computers, to the easier access to high-performance computing systems, and to the significant progress that has been made in numerical methods. Moreover, the understanding of the advantages and difficulties of the method (especially with regard to the convergence problems discussed above) has increased considerably in recent years. The FWI method is thus becoming the method of choice for the inversion of USCT data for breast and soft tissues imaging (Pérez-Liva et al. 2017), and we bet that this can also become the case for the imaging of bones in the medium term.

11.4. Conclusion

Ultrasound Computed Tomography (USCT) of bone tissue is still too limited today to be used in clinical applications. However, it should be possible to achieve this goal in the near future. In its simple and fast computerized version, as part of Born approximation, we have shown how to perform wide-band USCT of the cortical diaphysis of a long bone and how to obtain cross-sections in the spatial frequency plane. Real experiments using mechanical and electronic control systems show that the method can be successfully applied *in vitro*. Various enhancement paths can be explored: increase in the number of array elements, irregular distribution of transducers to increase the number of independent projections (compressive sensing, statistical estimators), adaptive signal and image processing based for example on deep learning, etc., and/or other inversion algorithms, such as iterative algorithms adapted to non-linear inversion. The fundamental limits of non-linear inversion algorithms, such as the so-called “full-waveform inversion” methods, must be overcome. It will be necessary to move away from fluid modeling schemes and introduce elastic modeling. For anatomical imaging of the cortical interfaces of bone and surrounding soft tissue, including marrow, fluid-like modeling may be sufficient to provide high resolutions. For the identification of biomechanical information of the bone, we will have to take into account the shear waves, and obtain a quantitative image of the whole organ. Today, this is still too complicated (or numerically unstable) to be envisaged on experimental laboratory data, and very far from a clinical application. But if the scientific community takes up the challenge, then USCT will truly be the efficient and indispensable modality.

11.5. Acknowledgements

The authors would like to thank Laurent Sabatier of the Laboratoire de Mécanique et d’Acoustique (LMA), and the Fédération de Recherche *Fabri de Peiresc*, Marseille, France. The authors also thank Laure Balasse and Samantha Fernandez of the European Centre for Research in Medical Imaging (CERIMED), Marseille, France.

11.6. References

- André, Michael P., J. Duncan Craven, Moses A. Greenfield, and Richard Stern. 1980. ‘Measurement of the Velocity of Ultrasound in the Human Femur *in Vivo*’. *Medical Physics* 7 (4): 324–30. <https://doi.org/10.1118/1.594713>.
- André, Michael P., Peter J. Martin, Gregory P. Otto, Linda K. Olson, Todd K. Barrett, Brett A. Spivey, and Douglas A. Palmer. 1995. ‘A New Consideration of Diffraction Computed Tomography for Breast Imaging: Studies in Phantoms and Patients’. In *Acoustical Imaging*, edited by Joie Pierce Jones, 379–90. Boston, MA: Springer US. https://doi.org/10.1007/978-1-4615-1943-0_40.
- Bamberger, A., G. Chavent, Ch. Hemon, and P. Lailly. 1982. ‘Inversion of Normal Incidence Seismograms’. *GEOPHYSICS* 47 (5): 757–70. <https://doi.org/10.1190/1.1441345>.
- Belkebir, Kamal, and Marc Saillard. 2004. ‘Testing Inversion Algorithms against Experimental Data: Inhomogeneous Targets’. *Inverse Problems* 21 (6): S1–3. <https://doi.org/10.1088/0266-5611/21/6/S01>.
- Berg, Peter M van den, and Ralph E Kleinman. 1997. ‘A Contrast Source Inversion Method’. *Inverse Problems* 13 (6): 1607–20. <https://doi.org/10.1088/0266-5611/13/6/013>.
- Bernard, Simon, Vadim Monteiller, Dimitri Komatitsch, and Philippe Laysgues. 2017. ‘Ultrasonic Computed Tomography Based on Full-Waveform Inversion for Bone Quantitative Imaging’. *Physics in Medicine & Biology* 62 (17): 7011–35. <https://doi.org/10.1088/1361-6560/aa7e5a>.
- Carson, Paul L. 1977. ‘Imaging Soft Tissue through Bone with Ultrasound Transmission Tomography by Reconstruction’. *Medical Physics* 4 (4): 302. <https://doi.org/10.1118/1.594318>.
- Chew, Weng Cho. 1995. *Waves and Fields in Inhomogeneous Media*. IEEE Press Series on Electromagnetic Waves. Piscataway, NY: IEEE Press.
- Crocco, Lorenzo, and Tommaso Isernia. 2001. ‘Inverse Scattering with Real Data: Detecting and Imaging Homogeneous Dielectric Objects’. *Inverse Problems* 17 (6): 1573–83. <https://doi.org/10.1088/0266-5611/17/6/302>.
- Deans, Stanley R. 2007. *The Radon Transform and Some of Its Applications*. Mineola, N.Y: Dover Publications.

Delamare, S., J. P. Lefebvre, and P. Lasaygues. 1997. ‘Back Scattered Ultrasonic Tomography: Experiments and Modelizations’. In *Acoustical Imaging*, edited by Sidney Lees and Leonard A. Ferrari, 23:595–600. Boston, MA: Springer US. http://link.springer.com/10.1007/978-1-4419-8588-0_93.

Dera, Dimah, Nidhal Bouaynaya, and Hassan M. Fathallah-Shaykh. 2016. ‘Automated Robust Image Segmentation: Level Set Method Using Nonnegative Matrix Factorization with Application to Brain MRI’. *Bulletin of Mathematical Biology* 78 (7): 1450–76. <https://doi.org/10.1007/s11538-016-0190-0>.

Deti, Valérie, Djilali Kourtiche, and M Nadi. 2002. ‘Acoustical Characterization of Bone Using a Cylindrical Model and Time of Flight Method: Edge Reconstruction and Ultrasound Velocity Determination in Cortical Bone and in Medullar Marrow’. *Physiological Measurement* 23 (2): 313–24. <https://doi.org/10.1088/0967-3334/23/2/307>.

Devaney, Anthony J. 2012. *Mathematical Foundations of Imaging, Tomography and Wavefield Inversion*. Cambridge: Cambridge University Press. <https://doi.org/10.1017/CBO9781139047838>.

Diong, M. L., A. Roueff, P. Lasaygues, and A. Litman. 2015. ‘Precision Analysis Based on Cramer–Rao Bound for 2D Acoustics and Electromagnetic Inverse Scattering’. *Inverse Problems* 31 (7): 075003. <https://doi.org/10.1088/0266-5611/31/7/075003>.

Diong, M L, A Roueff, P Lasaygues, and A Litman. 2016. ‘Impact of the Born Approximation on the Estimation Error in 2D Inverse Scattering’. *Inverse Problems* 32 (6): 065006. <https://doi.org/10.1088/0266-5611/32/6/065006>.

Duchêne, B. 2001. ‘Inversion of Experimental Data Using Linearized and Binary Specialized Nonlinear Inversion Schemes’. *Inverse Problems* 17 (6): 1623–34. <https://doi.org/10.1088/0266-5611/17/6/306>.

Duric, Nebojsa, Peter Littrup, Lou Poulo, Alex Babkin, Roman Pevzner, Earle Holsapple, Olsi Rama, and Carri Glide. 2007. ‘Detection of Breast Cancer with Ultrasound Tomography: First Results with the Computed Ultrasound Risk Evaluation (CURE) Prototype: Detection of Breast Cancer with Ultrasound Tomography’. *Medical Physics* 34 (2): 773–85. <https://doi.org/10.1118/1.2432161>.

Espinosa, Luis, Elise Doveri, Simon Bernard, Vadim Monteiller, Régine Guillermin, and Philippe Lasaygues. 2021. ‘Ultrasonic Imaging of High-Contrasted Objects Based on Full-Waveform Inversion: Limits under Fluid Modeling’. *Ultrasonic Imaging* 43 (2): 88–99. <https://doi.org/10.1177/0161734621990011>.

Falardeau, Timothe, and Pierre Belanger. 2018. ‘Ultrasound Tomography in Bone Mimicking Phantoms: Simulations and Experiments’. *The Journal of the Acoustical Society of America* 144 (5): 2937–46. <https://doi.org/10.1121/1.5079533>.

Fradi, Marwa, Wajih Elhadj Youssef, Philippe Lasaygues, and Mohsen Machhout. 2018. ‘Improved USCT of Paired Bones Using Waveletbased Image Processing’. *International Journal of Image, Graphics and Signal Processing* 10 (9): 1–9. <https://doi.org/10.5815/ijgisp.2018.09.01>.

Fradi, Marwa, Philippe Lasaygues, and Mohsen Machhout. 2019. ‘Auto-Organiser Neural Network Application for Ultrasound Computed Tomographic Image Classification’. In *2019 19th International Conference on Sciences and Techniques of Automatic Control and Computer Engineering (Sta)*, 19–23.

Franceschini, Emilie, Serge Mensah, Loïc Le Marrec, and Philippe Lasaygues. 2007. ‘An Optimization Method for Quantitative Impedance Tomography’. *IEEE Transactions on Ultrasonics, Ferroelectrics, and Frequency Control* 54 (8): 1578–88.

Greenleaf, J. F., S. A. Johnson, W. F. Samayoa, and F. A. Duck. 1975. ‘Algebraic Reconstruction of Spatial Distributions of Acoustic Velocities in Tissue from Their Time-of-Flight Profiles’. In *Acoustical Holography*, edited by Newell Booth, 71–90. Boston, MA: Springer US. http://link.springer.com/10.1007/978-1-4615-8216-8_4.

Greenleaf, James F., and Robert C. Bahn. 1981. ‘Clinical Imaging with Transmissive Ultrasonic Computerized Tomography’. *IEEE Transactions on Biomedical Engineering* BME-28 (2): 177–85. <https://doi.org/10.1109/TBME.1981.324789>.

Guillermin, Régine, Philippe Lasaygues, and Guy Rabau. 2015. ‘Quantitative Ultrasonic Imaging of Bones’. In *The 22nd International Congress on Sound and Vibration*, 1–6. IIAV. Florence, Italy: IIAV.

Guillermin, Régine, Philippe Lasaygues, Guy Rabau, and Jean-Pierre Lefebvre. 2013. ‘Quantitative Non-Linear Ultrasonic Imaging of Targets with Significant Acoustic Impedance Contrast—An Experimental Study’. *The Journal of the Acoustical Society of America* 134 (2): 1001–10. <https://doi.org/10.1121/1.4812778>.

Haddadin, O.S., and E.S. Ebbini. 1998. ‘Imaging Strongly Scattering Media Using a Multiple Frequency Distorted Born Iterative Method’. *IEEE Transactions on Ultrasonics, Ferroelectrics and Frequency Control* 45 (6): 1485–96. <https://doi.org/10.1109/58.738288>.

- Haddadin, Osama S., and Emad S. Ebbini. 1997. 'Multiple Frequency Distorted Born Iterative Method for Tomographic Imaging'. In *Acoustical Imaging*, edited by Sidney Lees and Leonard A. Ferrari, 23:613–19. Acoustical Imaging. Boston, MA: Springer US. https://doi.org/10.1007/978-1-4419-8588-0_96.
- Hongqiao, Li, and Wang Shengqian. 2009. 'A New Image Denoising Method Using Wavelet Transform'. In , 111–14. IEEE. <https://doi.org/10.1109/IFITA.2009.47>.
- Hopp, Torsten, Nicole Ruiter, Jeffrey C. Bamber, Neb Duric, and Koen W.A. Van Dongen. 2018. 'Proceedings of the International Workshop on Medical Ultrasound Tomography: 1.- 3. Nov. 2017, Speyer, Germany'. KIT Scientific Publishing. <https://doi.org/10.5445/KSP/1000071328>.
- Jose, A., S. Ravi, and M. Sambath. 2014. 'Brain Tumor Segmentation Using K-Means Clustering and Fuzzy C-Means Algorithm and Its Area Calculation'. *International Journal of Innovative Research in Computer and Communication Engineering*, 2014, Vol.2 edition.
- Kak, A., and M. Slaney. 2001. *Principles of Computerized Tomographic Imaging*. Society of Industrial and Applied Mathematics (SIAM).
- Lasaygues, P., J. P. Lefebvre, and S. Mensah. 1997. 'High Resolution Low Frequency Ultrasonic Tomography'. *Ultrasonic Imaging* 19 (4): 278–93.
- Lasaygues, P., D. Tanne, S. Mensah, and J.P. Lefebvre. 2002. 'Circular Antenna for Breast Ultrasonic Diffraction Tomography'. *Ultrasonic Imaging* 24 (3): 177–89. <https://doi.org/10.1177/016173460202400304>.
- Lasaygues, Philippe. 2006. 'Assessing the Cortical Thickness of Long Bone Shafts in Children, Using Two-Dimensional Ultrasonic Diffraction Tomography'. *Ultrasound in Medicine & Biology* 32 (8): 1215–27. <https://doi.org/10.1016/j.ultrasmedbio.2006.04.011>.
- Lasaygues, Philippe, Régine Guillermin, and Jean-Pierre Lefebvre. 2006. 'Distorted Born Diffraction Tomography Applied to Inverting Ultrasonic Field Scattered by Noncircular Infinite Elastic Tube'. *Ultrasonic Imaging* 28 (4): 211–29.
- Lasaygues, Philippe, Régine Guillermin, Khaled Metwally, Samantha Fernandez, Laure Balasse, Philippe Petit, and Cécile Baron. 2017. 'Contrast Resolution Enhancement of Ultrasonic Computed Tomography Using a Wavelet-Based Method – Preliminary Results in Bone Imaging'. In *Proceedings of the Int. Workshop on Medical Ultrasound Tomography*, 291–302. Speyer, Germany: Ed. J. Bamber, K.W.A. van Dongen, N. Duric, T. Hopp, N.V. Ruiter.

Lasaygues, Philippe, and Loïc Le Marrec. 2008. 'Ultrasonic Reflection Tomography vs. Canonical Body Approximation: Experimental Assessment of an Infinite Elastic Cylindrical Tube'. *Ultrasonic Imaging* 30 (1): 29–43.

Lasaygues, Philippe, Khaled Metwally, Régine Guillermin, Philippe Petit, and Cécile Baron. 2018. 'Dual-Frequency Cylindrical-Focusing Antenna for Contrast Enhanced Ultrasonic Computed Tomography of Paired Bones'. In *3rd International Conference on Ultrasonic-Based Applications - Ultrasonics 2018*, 60–62. Caparica, Portugal: Ed. C. Lodeiro, J.-L. Capelo.

Lasaygues, Philippe, Edgard Ouedraogo, Jean-Pierre Lefebvre, Marcel Gindre, Marilynne Talmant, and Pascal Laugier. 2005. 'Progress towards in Vitro Quantitative Imaging of Human Femur Using Compound Quantitative Ultrasonic Tomography'. *Physics in Medicine and Biology* 50 (11): 2633–49. <https://doi.org/10.1088/0031-9155/50/11/013>.

Lavarello, R.J., and M.L. Oelze. 2009. 'Tomographic Reconstruction of Three-Dimensional Volumes Using the Distorted Born Iterative Method'. *IEEE Transactions on Medical Imaging* 28 (10): 1643–53. <https://doi.org/10.1109/TMI.2009.2026274>.

Lavarello, Roberto, and Michael Oelze. 2008. 'A Study on the Reconstruction of Moderate Contrast Targets Using the Distorted Born Iterative Method'. *IEEE Transactions on Ultrasonics, Ferroelectrics and Frequency Control* 55 (1): 112–24. <https://doi.org/10.1109/TUFFC.2008.621>.

Lefebvre, J. P., P. Lasaygues, S. Mensah, S. Delamare, and A. Wirgin. 2002. 'Born Ultrasonic Tomography: Some Limits and Improvements'. In *Acoustical Imaging*, edited by Michael Halliwell and Peter N. T. Wells, 25:79–86. Boston: Kluwer Academic Publishers. http://link.springer.com/10.1007/0-306-47107-8_10.

Lefebvre, Jean-Pierre, Philippe Lasaygues, and Serge Mensah. 2009. 'Acoustic Tomography, Ultrasonic Tomography'. In *Materials and Acoustics Handbook*, edited by Michel Bruneau and Catherine Potel, 887–906. London, UK: ISTE. <http://doi.wiley.com/10.1002/9780470611609.ch35>.

Litman, Amélie, and Lorenzo Crocco. 2009. 'Testing Inversion Algorithms against Experimental Data: 3D Targets'. *Inverse Problems* 25 (2): 020201. <https://doi.org/10.1088/0266-5611/25/2/020201>.

Liu, Shuo. 2011. 'Image Segmentation Technology of the Ostu Method for Image Materials Based on Binary PSO Algorithm'. In *Advances in Computer Science, Intelligent System and Environment*, edited by David Jin and Sally

Lin, 104:415–19. Berlin, Heidelberg: Springer Berlin Heidelberg. https://doi.org/10.1007/978-3-642-23777-5_68.

Lobel, P., R.E. Kleinman, Ch. Pichot, L. Blanc-Feraud, and M. Barlaud. 1996. ‘Conjugate-Gradient Method for Solving Inverse Scattering with Experimental Data’. *IEEE Antennas and Propagation Magazine* 38 (3): 48. <https://doi.org/10.1109/MAP.1996.511954>.

Loosvelt, Matthieu, and Philippe Lasaygues. 2011. ‘A Wavelet-Based Processing Method for Simultaneously Determining Ultrasonic Velocity and Material Thickness’. *Ultrasonics* 51 (3): 325–39. <https://doi.org/10.1016/j.ultras.2010.10.006>.

Lu, C., J. Lin, W. Chew, and G. Otto. 1996. ‘Image Reconstruction with Acoustic Measurement Using Distorted Born Iteration Method’. *Ultrasonic Imaging* 18 (2): 140–56. <https://doi.org/10.1177/016173469601800204>.

Malagon Torres, Juan Sebastian, Jonathan Avendano Prez, Flavio Augusto Prieto, and Philippe Lasaygues. 2019. ‘Linear Filtering Method for Bone Structures in Computerized Ultrasonic Tomography Images’. In *Proceedings of STSIVA*, 1:1–4. Bucaramanga, Santander, Colombia: Universidad Industrial de Santander.

Mallat, S., and W.L. Hwang. 1992. ‘Singularity Detection and Processing with Wavelets’. *IEEE Transactions on Information Theory* 38 (2): 617–43. <https://doi.org/10.1109/18.119727>.

Marwa, Fradi, Wajih Elhadj Youssef, Mohsen Machhout, Philippe Petit, Cecile Baron, Regine Guillermin, and Philippe Lasaygues. 2019. ‘Automatic Recognition Processing in Ultrasound Computed Tomography of Bone’. In *Medical Imaging 2019: Ultrasonic Imaging and Tomography*, edited by B. C. Byram and N. V. Ruiter, 10955:UNSP 1095514. <https://doi.org/10.1117/12.2506473>.

Mayer, Markus A., Anja Borsdorf, Martin Wagner, Joachim Hornegger, Christian Y. Mardin, and Ralf P. Tornow. 2012. ‘Wavelet Denoising of Multiframe Optical Coherence Tomography Data’. *Biomedical Optics Express* 3 (3): 572. <https://doi.org/10.1364/BOE.3.000572>.

Mensah, S., and R. Ferriere. 2002. ‘Near-Field Diffraction Tomography’. *Ultrasonic Imaging* 24 (1): 13–24. <https://doi.org/10.1177/016173460202400102>.

Mensah, S., and R. Ferriere. 2004. ‘Diffraction Tomography: A Geometrical Distortion Free Procedure’. *Ultrasonics* 42 (1–9): 677–82. <https://doi.org/10.1016/j.ultras.2003.11.012>.

Metwally, Khaled, Emmanuelle Lefevre, Cécile Baron, Rui Zheng, Martine Pithioux, and Philippe Lasaygues. 2015. ‘Measuring Mass Density and Ultrasonic Wave Velocity: A Wavelet-Based Method Applied in Ultrasonic Reflection Mode’. *Ultrasonics*, September. <https://doi.org/10.1016/j.ultras.2015.09.006>.

Migeon, B., R. Charreyron, P. Deforge, A. Langlet, J. Renard, and P. Marché. 1998. ‘P031 An Automatic Spline-Based Contour Interpolation for the 3D Reconstruction of a Thin Walled Elastic Tube’. *Journal of Biomechanics* 31 (July): 70. [https://doi.org/10.1016/S0021-9290\(98\)80142-5](https://doi.org/10.1016/S0021-9290(98)80142-5).

Ouedraogo, E., P. Lasaygues, J. P. Lefebvre, M. Gindre, M. Talmant, and P. Laugier. 2002. ‘Contrast and Velocity Ultrasonic Tomography of Long Bones’. *Ultrasonic Imaging* 24 (3): 139–60.

Pérez-Liva, M., J. L. Herraiz, J. M. Udías, E. Miller, B. T. Cox, and B. E. Treeby. 2017. ‘Time Domain Reconstruction of Sound Speed and Attenuation in Ultrasound Computed Tomography Using Full Wave Inversiona)’. *The Journal of the Acoustical Society of America* 141 (3): 1595–1604. <https://doi.org/10.1121/1.4976688>.

Renaud, Guillaume, Pieter Kruizinga, Didier Cassereau, and Pascal Laugier. 2018. ‘In Vivo Ultrasound Imaging of the Bone Cortex’. *Physics in Medicine & Biology* 63 (12): 125010. <https://doi.org/10.1088/1361-6560/aac784>.

Rouyer, Julien, Philippe Lasaygues, and Serge Mensah. 2012. ‘Novel Ultrasound Tomograph for Anatomical Inspection’. In *Acoustical Imaging*, edited by Andrzej Nowicki, Jerzy Litniewski, and Tamara Kujawska, 31:3–10. Dordrecht: Springer Netherlands. http://www.springerlink.com/index/10.1007/978-94-007-2619-2_1.

Salehi, Leili. 2017. ‘Nonlinear Tomographic Reconstruction of Elastic Properties of Isotropic Solid Materials from Ultrasound Measurements’. Doctoral thesis, Ruhr-Universität Bochum, Universitätsbibliothek.

Scotti, T, and A Wirgin. 1995. ‘Shape Reconstruction Using Diffracted Waves and Canonical Solutions’. *Inverse Problems* 11 (5): 1097–1111. <https://doi.org/10.1088/0266-5611/11/5/013>.

Sehgal, C.M., D.G. Lewallen, J.A. Nicholson, R.A. Robb, and J.F. Greenleaf. 1988. ‘Ultrasound Transmission and Reflection Computerized Tomography for Imaging Bones and Adjoining Soft Tissues’. In , 849–52. IEEE. <https://doi.org/10.1109/ULTSYM.1988.49497>.

Shortell, Matthew P., Marwan A. M. Althomali, Marie-Luise Wille, and Christian M. Langton. 2017. ‘Combining Ultrasound Pulse-Echo and Transmission Computed Tomography for Quantitative Imaging the Cortical Shell of Long-Bone Replicas’. *Frontiers in Materials* 4 (November): 40. <https://doi.org/10.3389/fmats.2017.00040>.

Tijhuis, Anton G, Kamal Belkebir, Amélie C S Litman, and Bastiaan P de Hon. 2001. ‘Multiple-Frequency Distorted-Wave Born Approach to 2D Inverse Profiling’. *Inverse Problems* 17 (6): 1635–44. <https://doi.org/10.1088/0266-5611/17/6/307>.

Virieux, J., and S. Operto. 2009. ‘An Overview of Full-Waveform Inversion in Exploration Geophysics’. *GEOPHYSICS* 74 (6): WCC1–26. <https://doi.org/10.1190/1.3238367>.

Wiskin, J. W., D. T. Borup, E. Iuanow, J. Klock, and Mark W. Lenox. 2017. ‘3-D Nonlinear Acoustic Inverse Scattering: Algorithm and Quantitative Results’. *IEEE Transactions on Ultrasonics, Ferroelectrics, and Frequency Control* 64 (8): 1161–74. <https://doi.org/10.1109/TUFFC.2017.2706189>.

Wiskin, James W., Bilal Malik, Rajni Natesan, Nasser Pirshafiey, John Klock, and Mark Lenox. 2019. ‘3D Full Inverse Scattering Ultrasound Tomography of the Human Knee (Conference Presentation)’. In *Medical Imaging 2019: Ultrasonic Imaging and Tomography*, edited by Nicole V. Ruiter and Brett C. Byram, 25. San Diego, United States: SPIE. <https://doi.org/10.1117/12.2512595>.

Zheng, Rui, and Philippe Lasaygues. 2013. ‘Simultaneous Assessment of Bone Thickness and Velocity for Ultrasonic Computed Tomography Using Transmission-Echo Method’. In , 2084–87. IEEE. <https://doi.org/10.1109/ULTSYM.2013.0532>.